# Polar surface of ferroelectric nanodomains in GeTe thin films

B. Croes, F. Cheynis, P. Müller, S. Curiotto, and F. Leroy*
*Aix Marseille Univ, CNRS, CINAM, AMUTECH, Marseille, France*

(Received 31 March 2022; revised 20 May 2022; accepted 27 May 2022; published 9 June 2022)

Ferroelectrics have polar surfaces that can undergo large structural and stoichiometric modifications to be neutral. These changes can have major implications on the surface stability and physicochemical properties. We have studied the growth and structure of ferroelectric GeTe thin films on Si(111) by a combination of scanning tunneling microscopy, low-energy electron microscopy, and low-energy electron diffraction. We show that GeTe growth occurs with a single epitaxy and proceeds via a step-flow mode hindered by the advance of electrically neutral step edges exhibiting triangular notches. We demonstrate the presence of ferroelectric nanodomains with in-plane components of polarization and a complex restructuring of their polar surface. $2\times2$ surface reconstruction, missing row reconstruction and extended 2D modulations of the surface structure are demonstrated on these nanodomains. We show that these structures stabilize the surface termination of the low-symmetry polar nanodomains.

DOI: 10.1103/PhysRevMaterials.6.064407

Ferroelectric thin films are the object of intense fundamental research stimulated by their applications as functional materials based on the existence of different polar variants. The main factors that govern the spatial organization of ferroelectric domains are the elastic interactions that arise from the electromechanical coupling between domains and the electrostatic interactions due to local exceeding charges. The ability to synthesize ferroelectric thin films of high crystalline quality based on layer-by-layer growth techniques and to engineer the strain field *via* the substrate choice have made it possible to exploit these interactions and discover unique phenomena. It has been demonstrated that flux-closure polar domains [1–3], vortices [4,5], and even skyrmions [6] could be obtained in ferroelectric materials. This has led to a renewed interest [7–9] in prior studies on incommensurate phases in ferroelectrics with the observation of one-dimensional stripe domain patterns or even more complex 2D modulations as observed in the structural phase transitions of $\alpha$-$\beta$ quartz [10]. The experimental studies of the structure of ferroelectric materials are mainly based on the atomic scale characterization of domain boundaries and interfaces by scanning transmission electron microscopy [11] and x-ray diffraction [12,13]. The surface structure of ferroelectrics has been much less explored. However, the surface is also a place where charge screening and stress relaxation occur on atomic-scale distances. In particular, it has been recognized for a long time that a polar surface, i.e., a surface cut perpendicular to a direction along which the unit cell carries a net electric dipole moment, requires major rearrangements to solve the problem of the divergence of the electrostatic potential [14]. Several charge compensation mechanisms have been proposed to stabilize polar surfaces: purely electronic effects, modifications of the surface structure and/or stoichiometry or adsorption/segregation of charged species [15]. Moreover, since the polarization and strain gradient can couple together at the surface through the flexoelectric effect, we can expect that surface modulations or ripples can be favored [16,17]. Therefore, surface studies may provide insight into the fundamental properties of ferroelectric materials and this point is all the more crucial that mass transport processes during thin film growth occur at surfaces and may be strongly influenced by these surface modifications [18,19].

Among ferroelectrics, a class of materials with high potentialities for spintronic applications has been introduced, known as ferroelectric Rashba semiconductors [20]. Major results have been obtained on $\alpha$-GeTe thin films. The reversal of the ferroelectric polarization under an electric field [21] and a consistent change of the spin chirality of the band structure have been demonstrated [22,23]. The $\alpha$-GeTe ferroelectric phase has a rhombohedral structure (space group *R3m*) and bulk Curie temperature of $T_C \sim 650 - 700$ K. The spontaneous polarization of $\alpha$-GeTe is along the pseudocubic $\langle 111 \rangle$, leading to the formation of four ferroelastic variants and three possible polarization switching between domains at 71°, 109°, or 180°. As reported by Wang *et al.* [24], $\alpha$-GeTe thin films can be grown on Si(111) by molecular beam epitaxy with a quasisingle crystalline order using a predeposition of 1 ML of Sb onto the substrate. Croes *et al.* [25] have shown that such $\alpha$-GeTe thin film is an ideal platform to study and control ferroelectric nanodomains as they are no more limited by grain boundaries. The $\alpha$-GeTe thin films are made of main domains with a ferroelectric polarization perpendicular to the surface, i.e., in the [111] direction, called *c* domains, and ferroelectric nanodomains with a majority of 71°-type domain walls, hereafter called *a* domains. In this paper, we address the surface morphology and structure of $\alpha$-GeTe thin films grown on Si(111). From low energy electron microscopy (LEEM) and scanning tunneling microscopy (STM) studies, we show that $\alpha$-GeTe thin films grow *via* a step-flow mode of Ge-Te bilayers. The growth velocity is limited by the advance of step edges exhibiting triangular notches. Atomic details of the

*leroy@cinam.univ-mrs.fr

 

polar surface of $\alpha$-GeTe indicate that the surface of the GeTe $c$ domains is unreconstructed and Te terminated. On the contrary, the polar surface of the ferroelectric $a$ domains exhibits complex restructuring of the surface: a 2×2 surface reconstruction that is Ge terminated, a missing row reconstruction, and a large scale 2D structure ($\sim$4×5 nm$^2$) that stabilizes the surface. We show that these atomic rearrangements involve large Te mass transfers.

## I. EXPERIMENTAL SECTION

Si(111) wafers (Siltronix; 550 $\mu$m thick; $\rho$=1–10 Ωcm) are first cleaned by acetone and ethanol rinsing before introduction in ultrahigh vacuum (UHV, $10^{-8}$ Pa). Then the substrates are degassed at 1000 K for 12 h, followed by repeated high-temperature annealing (1500 K) during a few minutes to obtain a clean 7×7 surface reconstruction. A deposition of 1 ML of Sb is performed on the Si(111) surface, forming the so-called Si(111)-$\sqrt{3}\times\sqrt{3}$-Sb reconstruction that greatly improves the crystalline quality of the GeTe layer. The GeTe thin films are grown by co-deposition of Ge (1175 °C) and Te (310 °C) in UHV at 275 °C and precharacterized by *in situ* RHEED. All the deposition sources are effusion cells from MBE-Komponenten Gmbh. After growth, the GeTe layers are transferred under UHV conditions thanks to a homemade transfer suitcase and characterized by LEEM, low energy electron diffraction (LEED) using a LEEM III microscope (Elmitec GmbH), and scanning tunneling microscopy (STM) by a VT-STM (Omicron Gmbh). LEEM images were obtained in bright field mode at an incident electron energy of 26 eV where a local maximum of reflectivity occurs. At this energy, the reflected electrons by the GeTe $c$ domains and by the tilted ferroelectric $a$ nanodomains are clearly separated in the focal plane. This allows to use the smallest contrast aperture (Ø=10 $\mu$m) to select only the reflected beam from the $c$ domains [see Fig. 1(a)]. STM images were obtained at room temperature in constant current mode with typical imaging conditions (U=−1 V, I= 20 pA, W tip). *In situ* STM characterization of the $a$-nanodomain evolution under thermal annealing was performed at constant temperature in the range 200–250 °C. The internal structure of GeTe thin films has been studied by x-ray diffraction at BM32 beamline (ESRF) and high-resolution TEM. X-ray diffraction data have been measured at 18 keV [0.06888 nm] with a beam size of 200×300 $\mu$m$^2$ and collected onto a 2D detector. The data analysis consists of a field correction (of the possible nonuniform response of the various pixels of the detector) and then a conversion of the measured data from the detector coordinates (pixel index) to diffraction angles and thus to reciprocal space coordinates [26]. The 3D reciprocal space maps were visualized using ParaView software. TEM investigations were performed along the $[1\bar{1}0]$ zone axis at an accelerating voltage of 300 kV on a JEOL JEM-3010 instrument with a spatial resolution of 0.17 nm.

## II. RESULTS AND DISCUSSION

### A. Growth and structure of *a* nanodomains

The surface morphology of a 470-nm-thick GeTe thin film grown on Si(111) is observed by LEEM [Fig. 1(a)]. It shows extended flat areas separated by depressions and needle-shaped $a$ nanodomains extended in the $\langle 1\bar{1}0\rangle$ direction in cubic coordinates of the Si substrate. The LEED pattern of the surface shows that the threefold symmetry [Fig. 1(b)i] can be associated with the growth of (111) planes of GeTe on Si(111). Using the diffracted spots for LEEM imaging (dark-field imaging mode), we see that only a small fraction of twinned grains are detected at the surface of the thin film (ACB stacking instead of ABC, see Figs. 1(b)ii and 1(b)iii]. These results indicate a majority epitaxy of $\alpha$-GeTe (111)‖Si(111) and $[1\bar{1}0]$‖Si$[1\bar{1}0]$ [24]. We can also detect by LEEM typical regular rows of defects on the terraces displaying a characteristic bright (dark) contrast [see dashed rectangles in Fig. 1(a)]. These structures have a period $L$ in the range 50–100 nm and extend over 0.2–1 $\mu$m distance. They are characteristics of dislocations at small-angle grain boundaries that are associated with an azimuthal misorientation $\Delta\theta$ between two neighboring grains [27]. From the periodicity of the defects, we can estimate the local misorientation of the lattices as $\Delta\theta \sim \frac{a}{L} \sim 0.2^\circ - 0.4^\circ$ that is within the expected angular range deduced from x-ray measurements of the in-plane mosaicity [24]. The surface is also covered with elongated $a$ nanodomains. These nanodomains appear as dark needles in bright field LEEM imaging mode since the reflected beams from these $a$ domains are angularly distant. Indeed, the LEED pattern shows that the main reflected beam by the surface is surrounded by three additional secondary reflected beams [Fig. 1(e)]. Since the angular shift of these beams increases with the incident electron energy, they correspond to tilted surface planes [28]. Croes *et al.* [25] has shown that the tilt angle of the $a$ domains can be estimated as $1.4^\circ \pm 0.1^\circ$. These $a$ domains can also be observed in bulk by cross-section TEM showing the presence of 71°-type domain walls [Fig. 1(c)]. Moreover, the 3D reciprocal space map measured by x-ray diffraction around the $222_c$ Bragg peak ($c$ stands for pseudocubic coordinate) shows a splitting in four peaks. The major peak is at the lowest $q_z$ momentum transfer value (35.41 nm$^{-1}$) and can be assigned to the GeTe $c$ domains with a rhombohedral elongation of the unit cell in the [111] direction, i.e., perpendicular to the film ($q_z$ is perpendicular to the surface). The three minor peaks are localized at higher $q_z$ (36.73 nm$^{-1}$) and can be assigned to ferroelastic and/or ferroelectric $a$ nanodomains whose unit cells are stretched in the three remaining directions $[11\bar{1}]_c$, $[1\bar{1}1]_c$, and $[\bar{1}11]_c$ in pseudocubic coordinates. The $a$ domains have a polarization direction at 71° with respect to the surface normal, i.e., mainly in plane. This corroborates the observation that GeTe films have a preferential out-of-plane ferroelectric self-poling state dominated by $c$ domains [29].

In addition to domains and defects, LEEM measurements also show that the GeTe surface is made of atomically flat (111) terraces separated by atomic steps that are a few hundred nanometers away. Since no island is visible on the terraces, this indicates that GeTe growth on Si(111) occurs *via* a steady state step-flow mode. Therefore, during growth at 275 °y the diffusion length of the species before nucleation of a 2D island is larger than the typical terrace width (>100 nm). To better characterize the growth process, Fig. 2(a) shows a large-scale STM image (2×2 $\mu$m$^2$) of an 800-nm-thick GeTe film. LEEM and STM show similar surface features (see Supplemental

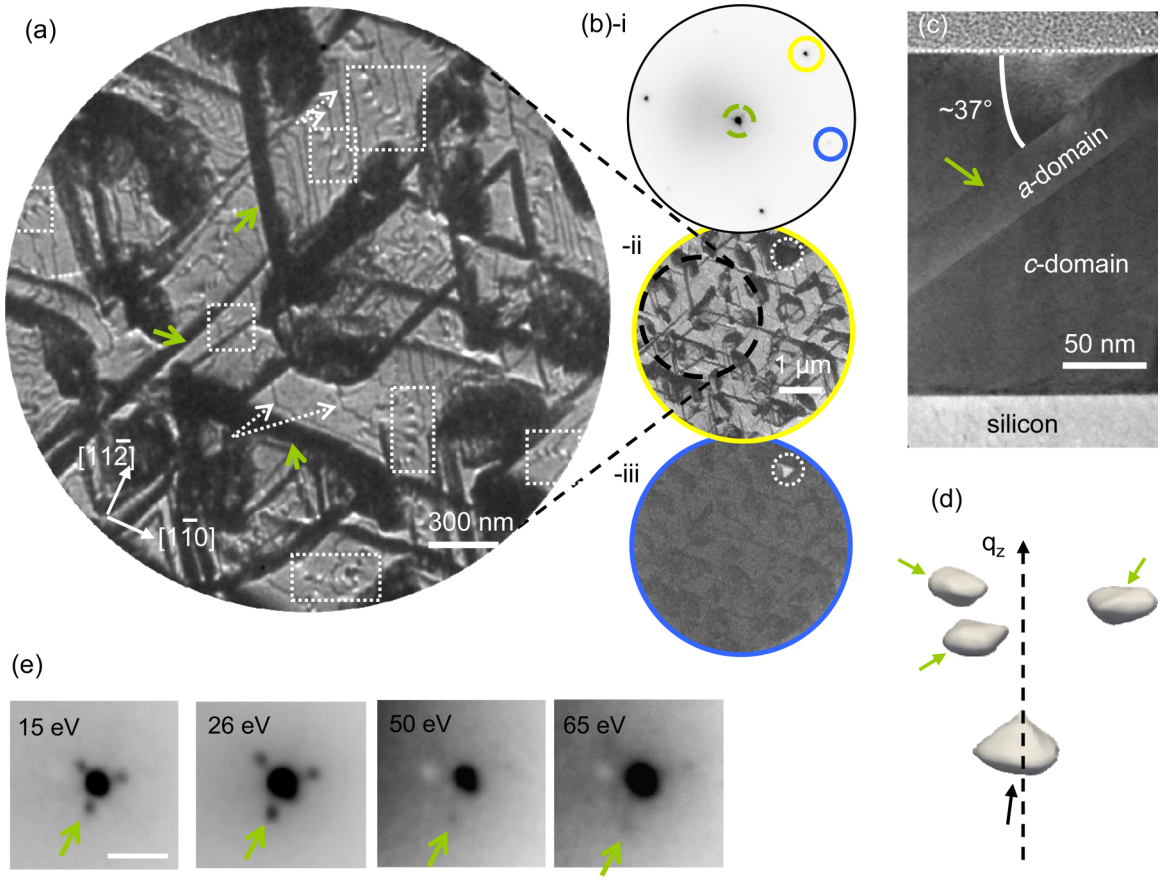


FIG. 1. (a) LEEM image of a 470-nm-thick GeTe thin film grown on Si(111)-$\sqrt{3}\times\sqrt{3}$-Sb (bright field mode, electron energy: 26 eV). The contrast aperture selects only the reflected beam from the *c* domains, excluding the reflected beams from the *a* nanodomains appearing as dark needles (green arrows). Row of defects from grain boundaries (see, for instance, in white dashed rectangles), ferroelectric *a* nanodomains (green arrows), atomic steps (white dashed arrows). (b)–(i) LEED pattern of GeTe thin film (electron energy: 26 eV; incident beam diameter: Ø=20 $\mu$m). The threefold symmetry of the pattern arises from the (111) surface structure of GeTe. (ii) LEEM image in dark field mode (electron energy: 26 eV), selecting the most intense diffracted beam [yellow circle in (i)]. (iii) LEEM image in dark field mode (electron energy: 26 eV) selecting the less intense diffracted beam [purple circle in (i)]. Twinned grain [white dotted circles in (ii) and (iii)].(c) TEM cross section of a 200-nm-thick GeTe thin film with medium resolution ([1$\bar{1}$0] zone axis). The green arrow shows a *a* nanodomain crossing the film. (d) Isointensity representation (40 000 counts) of a 3D reciprocal space map around (00$q_z$) at $q_z \sim 36$ nm$^{-1}$ (film thickness 800 nm). The green arrows show the diffraction peaks from the *a* domains. (e) Close view around the (00) reflected beam of a LEED pattern (electron energy: 26 eV) at incident electron energy E= 15, 26, 50 and 65 eV. The green arrows show the shift of the reflected beam by the *a* domains with the incident electron energy.

Material S1 [30]). The STM image derivative in Fig. 2(b) highlights the *a* nanodomains elongated in the $\langle 1\bar{1}0\rangle$ direction since the surface plane is tilted. As for LEEM images, three domain orientations coexist. The surface also shows the presence of atomic steps corresponding to single Ge-Te bilayers [0.35 nm, inset in Fig. 2(a)] as expected from the bulk lattice parameter of GeTe. This observation demonstrates that the GeTe growth proceeds *via* a direct incorporation of Ge and Te atoms at a bilayer step edge and not by successive growth of Ge and Te layers. This step-flow mode is associated with a well-defined orientation of atomic step edges with ascending steps in the $\langle\bar{1}\bar{1}2\rangle$ direction [Figs. 2(a) and 2(b)]. Considering a (111)-oriented surface, there exists two low-energy step edges, the so-called A- and B-step edges (pseudo-fcc crystals), with in-plane orientations differing by 60° [31]. Since B-step (respectively, A-step) edges are ascending (respectively, descending) in the $\langle\bar{1}\bar{1}2\rangle$ direction [Fig. 2(d)], thus the surface is dominated by B-step edges under growth conditions. From STM topography [see Fig. 2(e)], corresponding to an intermediary stage of thin film growth (before the steady-state step-flow process) both step edges can be observed on the surface. We can notice that A-step edges are straight whereas triangular notches are formed on B-step edges [see Fig. 2(e)]. Since at the late stage of the growth, all step edges are B type, we can infer that A-step edges grow faster than B-type [Fig. 2(c)]. The sketch of the atomic structure of the GeTe surface [Fig. 2(d)] shows that the A-step edge is made with a {100} microfacet whereas the B-step edge is made with a {111} microfacet. Therefore an A-step edge is stoichiometric in Ge-Te and is nonpolar whereas a B-step edge is made of a single element and polar. Since B-step edges exhibit triangular notches, they spontaneously decompose into A-step edges and have a step edge termination without net charges. In addition, the notches increase by a factor of 2 the step edge length of B

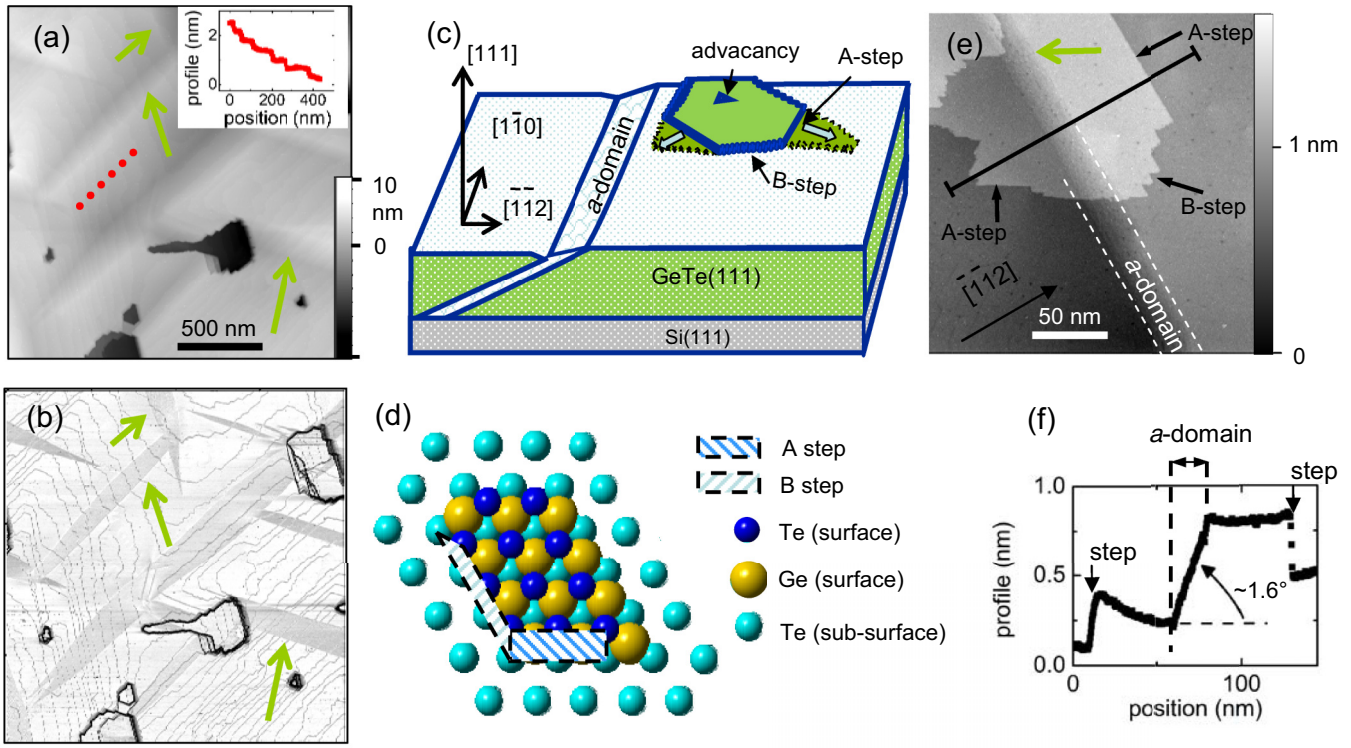


FIG. 2. (a) Large scale STM image of a 800 nm-thick GeTe thin film grown on Si(111)-$\sqrt{3}\times\sqrt{3}$-Sb (U= −1V; I= 20 pA). Green arrows show ferroelectric *a*-nanodomains. Inset: profile on STM image (a) along dashed lines showing atomic steps at the surface (1 GeTe Bilayer (BL)=0.35 nm). (b) Image derivative of (a) to highlight ferroelectric *a*-nanodomains and atomic steps. (c) Scheme of the surface morphology of GeTe thin films on Si(111). (d) Scheme of A-step and B-step edge models. (e) Close view by STM of a 80 nm-thick GeTe thin film grown on Si(111)-$\sqrt{3}\times\sqrt{3}$-Sb (U= -1V; I= 20 pA). Ferroelectric *a*-domains (green arrow and dotted guide lines), A-step and notched B-step edges (black arrows). (f) profile on STM image (e) (arrow: inclined profile due to the *a*-domain tilt).

steps with respect to a straight step edge, thus the growth rate of these notched B-step edge is reduced, which favors their presence at the surface during growth.

STM images reveal also that atomic steps are undisturbed by the ferroelectric *a* domains [see Figs. 2(a), 2(b) and 2(e)]. This observation is fully consistent with the result that the growth of GeTe thin films occurs at a sufficiently high temperature for the ferroelectric *a* domains to be absent [25]. The *a* nanodomains nucleate and grow during cooling to room temperature after thin film growth and do not modify the overall step organization. However, the ferroelectric *a* domains still have an influence on the morphology of the GeTe surface as the height profile in the neighborhood of the *a* domains is nonsymmetric [Figs. 2(e) and 2(f)]. The surface of the GeTe *c*-domains is lower on one side of the *a*-nanodomains (in the [11$\bar{2}$] direction) whereas it is higher and flat on the opposite side. This morphology is related to the difference of (111) inter-reticular distance $d_{111}$ between the *c* domains and the ferroelectric *a* nanodomains as well as the penetration angle of the *a* nanodomains inside the GeTe film. The inter-reticular distances $d_{111}$ can be directly compared from the position of the $222_c$ Bragg peaks measured by x-ray diffraction [Fig. 1(d)]. They provide a quantitative estimate of the compression of the (111) crystallographic planes (3.74%) inside the *a* nanodomains with respect to the *c* domains. Since the *a* nanodomains penetrate with a definite angle inside the film [see TEM in Fig. 1(c) for the 71°-type domain wall], then the lowering effect measured on the GeTe surface of *c* domains occurs on one side, i.e., above the ferroelectric *a* nanodomains, while it is absent on the other side. The domain wall angle (37°) and the film height *H* provide a typical distance *W* over which the deformation of the GeTe surface extends $W \sim \frac{H}{\tan(37°)} \sim 1.3H$.

### B. Surface polarity of *a* nanodomains

The ferroelectric *a* nanodomains allow relaxing the internal stress induced by the substrate into the GeTe thin film [25]. In addition to the epitaxial stress at the interface, the free surface may also relax and this point is all the more crucial for polar surfaces [14]. However, on the surface of the GeTe *c* domains, that is, polar, no surface reconstruction is detected by LEED or STM. This result corroborates previous STM observations of the surface of GeTe [32] and DFT calculations that a pristine (i.e., unreconstructed) Te-covered (111) surface is energetically favorable [33]. Considering the ferroelectric *a* nanodomains, microdiffraction measurements ($\mu$-LEED, beam diameter Ø=300 nm) on one single *a* nanodomain give some information on the crystallographic structure [Fig. 3(a)]. First, the shift of the reflected beam can be assigned to the local tilt angle (∼1.5° ± 0.2°) of the *a*-domain surface in the [11$\bar{2}$] direction with respect to the GeTe *c* domain [25]. This typical tilt angle is in adequation with the STM profile of the surface morphology [Fig. 2(f)] and corroborates macroscopic

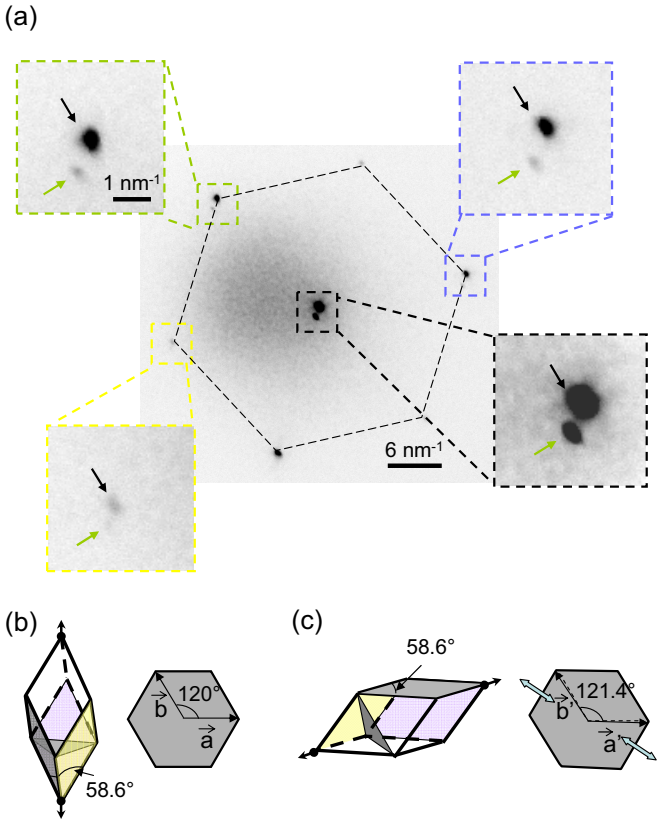


FIG. 3. (a) $\mu$-LEED pattern of a GeTe thin film (800 nm thick). The incident beam diameter is Ø=300 nm and the electron energy $E = 26$ V. The incident beam illuminates one ferroelectric $a$ nanodomain and the surrounding GeTe layer. The hexagonal pattern of GeTe surface structure of the $c$ domain is detected (dashed hexagon). Insets: Close views of reflected and diffracted spots. All spots are split into a major peak (black arrow) coming from the GeTe $c$-domain layer and a minor peak (green arrow) arising from the ferroelectric $a$ domain. The shift between the major and minor peaks is not a simple translation but changes with the selected diffracted spot). (b) Scheme of the crystallographic structure of GeTe $c$ domain and hexagonal surface lattice. (c) Same as (b) for a ferroelectric $a$ domain.

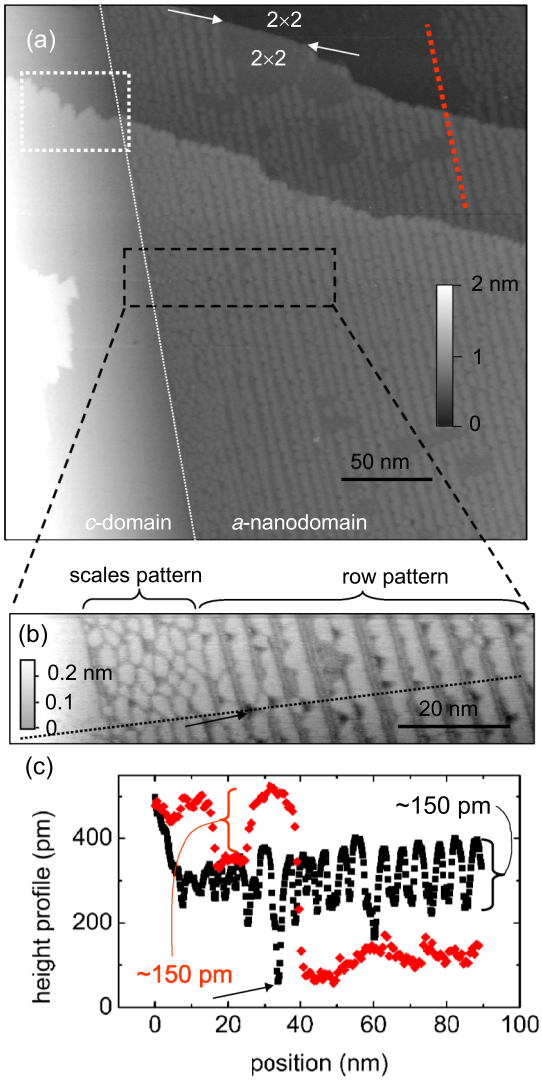


FIG. 4. (a) STM image (U= −1V; I= 20 pA) of the GeTe surface morphology (800-nm-thick film). A ferroelectric $a$ domain is on the right and the GeTe $c$ domain on the left. Flatness is imposed on the $a$-domain surface. Notched step edge on the main GeTe layer (white dashed rectangle). Straight step edge inside a 2×2 reconstructed area on the $a$ nanodomain (in between white arrows). (b) STM image (U = −1V; I = 20 pA) of the ferroelectric $a$ domain (from dashed rectangle on image (a)) with row and scale patterns. Black arrow shows a GeTe bilayer vacancy island. (c) STM height profiles along the 2×2 reconstruction [red doted line in (a)] and row pattern [black doted line in (b)]. The black arrow shows the dip into the profile at the bilayer vacancy island in (b).

measurements of the shift of the reflected beam by LEED [Fig. 1(e)]. Considering now the crystallographic lattice of the ferroelectric domains, it appears that the diffracted spots of the $a$ nanodomain do not coincide with those of the $c$ domains, even after correcting for the rigid shift due to the tilt angle [Fig. 3(a)]. To avoid systematic errors due to the distortion of the reciprocal space by the LEED setup, we compare only the positions of the reciprocal lattice points of the $a$ nanodomain and the $c$ domain that are localized in the same reciprocal space area. The reciprocal lattice of the $a$ nanodomain is slightly compressed by $2.2 \pm 0.2\%$ in the $[11\bar{2}]$ direction. We deduce that the in-plane lattice of the $a$ nanodomain is a distorted hexagon [Fig. 3(b)] with a monoclinic unit cell ($a' = b' = 0.427$ nm, angle = 121.4°) whereas the $c$-domains have a hexagonal unit cell ($a = 0.418$ nm, $b = 0.418$ nm, angle = 120°). This result also perfectly matches the lattice of the GeTe $a$ nanodomains measured by x-ray diffraction when these latter are elongated along $[11\bar{1}]$ and considering the (111) cut plane.

This result shows that the surface of the $c$ domains has a polarization axis aligned along the normal to the surface and a threefold symmetry whereas the surface plane of the $a$ nanodomains has a twofold symmetry axis. In addition, the surface normal of the $a$ nanodomains is not parallel to the elongation axis of the rhombohedron but tilted by ∼71°. To address the surface relaxation mechanisms of the polar $a$ nanodomains, we have performed high-resolution STM images. Surface images of an 800-nm-thick GeTe thin film show different features [Figs. 4(a) and 4(b)]. Flat areas are visible in

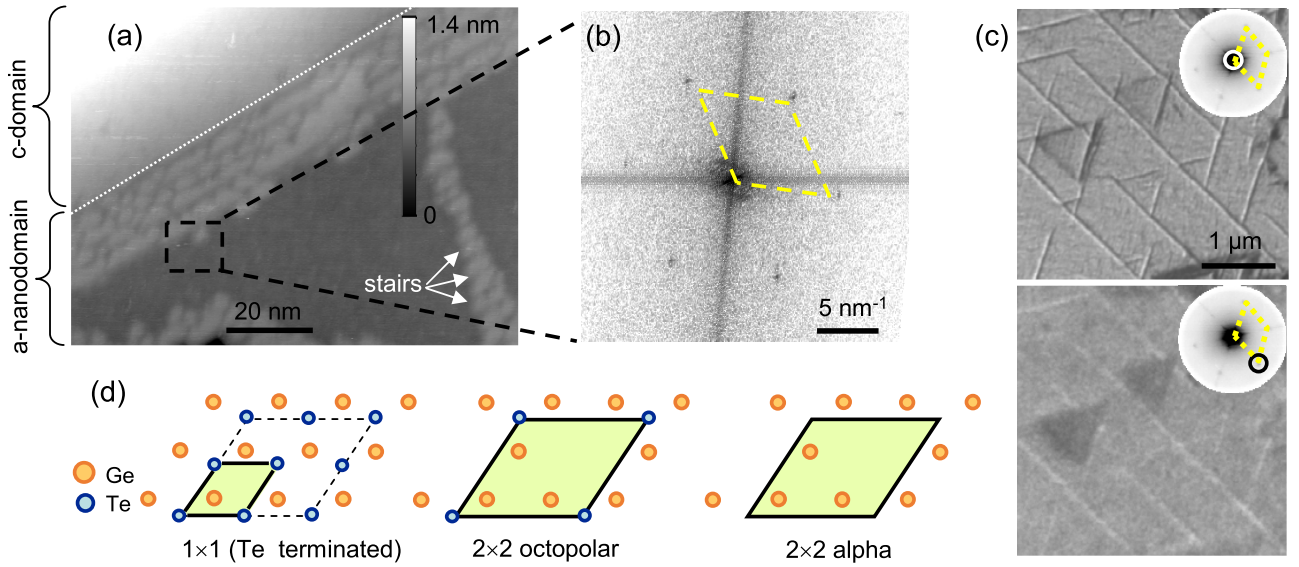


FIG. 5. (a) STM image of the surface of an *a* nanodomain of a 1500-nm-thick GeTe thin film grown on Si(111)-$\sqrt{3}\times\sqrt{3}$-Sb (U= −1V; I= 20 pA). (b) FFT of a high-resolution STM image of the flat area of an *a*-nanodomain showing a 2D hexagonal lattice. (c) Bright-field (top) and dark-field (bottom) LEEM images at 6 eV of a 460-nm-thick GeTe thin film. The bright field mode is obtained selecting the reflected beams from both *c* and *a* domains (white circle in LEED pattern). The *a* domains appear with a bright-dark contrast due to the hill-and-valley morphology (titled surface) and focusing conditions (see Ref. [45] and Supplemental Materials S7 and S8 in Ref. [25]). The dark field image is obtained selecting a 2×2 spot (dark circle in LEED pattern). Inset: $\mu$-LEED patterns showing fine 2×2 spots from a 2×2 surface reconstruction. (d) Geometric model of the surface structure of a flat zone: 1×1 Te terminated, 2×2 octopolar reconstruction, and 2×2 alpha reconstruction.

the middle of the *a* domain and regular rows are formed along the long side of the *a* domain, i.e., parallel to the [1$\bar{1}$0] direction. In addition, very close to the *a*-domain edge, the row structure changes to a two-dimensional structure described as a scales structure. To determine the chemical termination at the surface of the *a* nanodomains, we can compare the surface profiles of *a* and *c* domains. The flat areas of *a* nanodomains are ∼ 150 pm below the surface of *c* domains. This height corresponds approximately to the atomic spacing of the short Ge-Te bond [33]. Since *c* domains are known to be Te terminated, as deduced from XPS measurements [22] and surface energy minimization calculations [33], then the flat areas of *a* nanodomains must be Ge terminated. Concerning the row structure, it has a height modulation of 150± 20 pm and a periodicity of 5.1 ± 0.2 nm [Fig. 4(c)]. This height modulation can be attributed to a missing row reconstruction of Te. Such a 1D surface modulation is consistent with the translation invariance of the *c* domains along the long axis of the needle, i.e., in the [1$\bar{1}$0] direction. This missing row reconstruction is also observed in the context of metal surfaces with or without adsorption of adspecies (Pt(110) [34], Au(110) [35], O/Pd(110) [36]). The 2D scale structure observed initially close to the domain edge in Fig. 4(b) tends to cover the entire *a*-domain surface after long annealing at 200 °C under UHV and forms a highly regular 2D network. The scale structure is made of missing Te rows in two directions. In addition, triangular holes corresponding to GeTe bilayer vacancies can be found (∼ 320± 50 pm). They preferentially occur in between Te scales or at the side of missing rows of Te [see Fig. 4(b)].

Based on our STM observations, we have found that, kinetically, the surface termination of the ferroelectric *a* nanodomains changes with a well-defined process: (i) At first cooling, i.e., just after thin film growth, and for large *a* domains (>100 nm width), the surface of *a* domains show extended flat areas that are thus Ge terminated. (ii) Upon annealing, the surface of the domains equilibrate by first forming a row structure (missing row reconstruction) and then (iii) a scales pattern that orders at long distance. The initial stability of the Ge-terminated flat areas in the middle of the *a* domains may be counterintuitive considering surface energies [33]. Figures 5(a) and 5(b) show an atomically resolved STM image of a Ge-terminated flat area in the middle of an *a* nanodomain. From the Fourier transform of the height of the flat area, we can measure a hexagonallike pattern and a surface unit cell that is four times larger than the GeTe(111)-(1×1) bulk-terminated unit cell. Complementary $\mu$-LEED pattern at 6 eV incident energy shows that the surface is indeed 2×2 reconstructed and dark-field imaging with a 2×2 diffracted beam localizes the reconstruction on the *a* nanodomains corroborating the STM analysis [Fig. 5(c)]. This type of surface reconstruction has been suggested on a similar IV-VI semiconductor system PbTe(111) by Rutherford back scattering measurements [37]. A 2×2 reconstruction has also been proposed to neutralize polar surfaces in the context of ionic materials or semiconductors and is known as the octopolar or alpha reconstruction [38–41]. The octopolar reconstruction [42] is a pyramidlike structure obtained by keeping one-quarter of atoms from the surface layer and three quarters of atoms from the subsurface layer. The alpha reconstruction derives from the octopolar one by removing the last atom of the surface layer [see geometrical model in Fig. 5(d)]. From the analysis of the STM images that indicates a Ge-terminated surface, it is the alpha reconstruction that is observed on the *a*-domain surface. In addition, Deringer

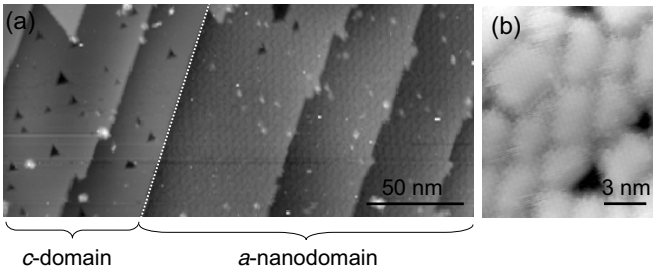


FIG. 6. (a) Large view STM image of the surface of an *a* nanodomain of a 800-nm-thick GeTe thin film under annealing at 220 °C (*a* nanodomain on the right side of the dashed line). (b) High-resolution STM image at RT of the scales structure onto a *a*-nanodomain surface. U = −1V; I = 20 pA.

*et al.* has theoretically shown [33] that the alpha and octopolar reconstructions have similar surface energies on a polar (111)-GeTe surface (respectively, 3.4–3.7 and 3.5 eV.nm$^{-2}$). Despite the fact that the Te-terminated unreconstructed surface is the most stable (surface energy: 1.5–2.1 eV nm$^{-2}$) and is observed on the (111)-GeTe *c* domains, it appears not to be the case on the *a* nanodomains. We can notice that this 2×2 reconstruction induces a drastic change in the chemical termination of the surface (Ge) and stoichiometry ($Ge_3Te_4$) that may deeply modify the electronic properties. In that respect, we can also notice that B-step edges crossing flat 2×2 zones have no notch on the contrary to B-step edges on the GeTe *c* domains [see Fig. 4(a) at the top]. This reinforces the proposal that the 2×2 surface reconstruction neutralizes the surface charges. The row pattern (Te terminated) on the *a* domains could be considered as a 12×1 surface reconstruction and may be compared to the 2×1 reconstruction (spinel reconstruction) as also theoretically predicted on polar (111)-GeTe surfaces [33] and detected by RHEED measurements on PbTe(111) thin films [43,44]. This reconstruction grows from the *a*-domain edges *via* stairs crossing the *a*-domain width [see Fig. 5(a)]. This growth mechanism shows that the advance of the reconstruction onto the surface is favored by the local environment of the atoms. At last, the scale pattern is a stable reconstruction that stays on the *a*-domain surface whatever further annealing or cooling processes. Figure 6(a) shows the surface of a GeTe *a* nanodomain held at 220 °C. The domain surface shows a regular pattern of scales where the periodicity increases with temperature whereas the GeTe *c* domains keep an unreconstructed surface with triangular *ad*vacancy islands coming from the GeTe congruent sublimation. The step-edge retraction phenomena favors the fastest step edges in terms of kinetics of mass transfers, i.e., A-step edges that are straight and neutral. Atomically resolved STM images of scales [Fig. 6(b)] show that this reconstruction has a very large unit cell (∼ 4×5 nm$^2$). We can deduce from the height profile that the surface is Te terminated with missing rows in two directions. To understand the observed changes of reconstructions, we infer that the 2×2 reconstruction and missing row pattern are metastable surface phases induced by a lack of Te. Indeed, as Te is much more volatile than Ge [46,47], we can expect that adsorbed Te onto the surface is the minority species during GeTe growth. Therefore the Te/Ge adatom ratio on the surface during deposition is slightly below 1. When growth is stopped and temperature decreased to room temperature, ferroelectric *a* domains nucleate and grow. This process is due to the different linear expansion coefficients of GeTe and Si that induce a thermomechanical stress inside the film [25]. The occurrence of the *a* nanodomains relaxes the global tensile stress by expanding the in-plane lattice parameter. Such a process only involves local rearrangements of atomic positions and the kinetics is expected to be much faster than mass transfers by diffusion. Consequently, it does not provide enough time for the species to diffuse over large distances and optimize all surface structures. As the surface of the *a* nanodomains and *c* domains are in competition for Te, we observe that Te free *ad*atoms primarily cover the *c* domains. The *a*-nanodomain surface is therefore Ge terminated and forms the 2×2 alpha reconstruction. After annealing the surface of *a* nanodomains equilibrates *via* Te bulk diffusion and forms successively a missing row reconstruction and a scale structure that are more and more Te rich. As the structures change from the domain edges, we can infer that the Te atoms segregate from the domain walls.

## III. CONCLUSION

In conclusion, we have studied the growth and structure of the polar surface of ferroelectric GeTe thin films epitaxially grown on Si(111). The surface of the ferroelectric *c* domains of GeTe has a rhombohedral elongation perpendicular to the surface and is unreconstructed. Considering the ferroelectric *a* nanodomains, the rhombohedral elongation is at 71° with respect to the surface normal. We have shown that the in-plane surface lattice is monoclinic and slightly tilted by 1.4° with respect to the *c* domains. The surface structure and polarity relax *via* a complex reorganization of surface atoms: a 2×2 alpha reconstruction, a missing row reconstruction, and a 2D modulated structure form successively upon annealing. These surface relaxations release the surface energy involved in this low-symmetry polar surface exhibiting a monoclinic unit cell and mainly a planar polarization. Our experimental measurements can be used as a playground to control ferroelectric domains and polarity in GeTe that will help to tune the surface Rashba effect *via* surface reconstructions.

## ACKNOWLEDGMENTS

The project leading to this publication received funding from Excellence Initiative of Aix-Marseille University A*MIDEX, a French Investissements d'Avenir program through the AMUtech lnstitute. This paper has also been supported by the ANR grant HOLOLEEM (Grant No. ANR-15-CE09-0012). We thank Martiane Cabié (CP2M, Marseille, France) for lamella preparation of GeTe thin films by FIB, Lucio Martinelli (Synchrotron ESRF, Grenoble, France) for x-ray measurements and Salia Cherifi-Hertel (IPCMS, Strasbourg, France) for fruitful discussions on ferroelectrics.

[1] A. Gruverman, D. Wu, H.-J. Fan, I. Vrejoiu, M. Alexe, R. J. Harrison, and J. F. Scott, Vortex ferroelectric domains, J. Phys.: Condens. Matter **20**, 342201 (2008).

[2] N. Balke, B. Winchester, W. Ren, Y. H. Chu, A. N. Morozovska, E. A. Eliseev, M. Huijben, R. K. Vasudevan, P. Maksymovych, J. Britson, S. Jesse, I. Kornev, R. Ramesh, L. Bellaiche, L. Q. Chen, and S. V. Kalinin, Enhanced electric conductivity at ferroelectric vortex cores in $BiFeO_3$, Nat. Phys. **8**, 81 (2012).

[3] Y. L. Tang, Y. L. Zhu, X. L. Ma, A. Y. Borisevich, A. N. Morozovska, E. A. Eliseev, W. Y. Wang, Y. J. Wang, Y. B. Xu, Z. D. Zhang, and S. J. Pennycook, Observation of a periodic array of flux-closure quadrants in strained ferroelectric $PbTiO_3$ films, Science **348**, 547 (2015).

[4] A. K. Yadav, C. T. Nelson, S. L. Hsu, Z. Hong, J. D. Clarkson, C. M. Schlepueetz, A. R. Damodaran, P. Shafer, E. Arenholz, L. R. Dedon, D. Chen, A. Vishwanath, A. M. Minor, L. Q. Chen, J. F. Scott, L. W. Martin, and R. Ramesh, Observation of polar vortices in oxide superlattices, Nature (London) **530**, 198 (2016).

[5] P. Shafer, P. Garcia-Fernandez, P. Aguado-Puente, A. R. Damodaran, A. K. Yadav, C. T. Nelson, S.-L. Hsu, J. C. Wojdel, J. Iniguez, L. W. Martin, E. Arenholz, J. Junquera, and R. Ramesh, Emergent chirality in the electric polarization texture of titanate superlattices, Proc. Natl. Acad. Sci. USA **115**, 915 (2018).

[6] S. Das, Y. L. Tang, Z. Hong, M. A. P. Goncalves, M. R. McCarter, C. Klewe, K. X. Nguyen, F. Gomez-Ortiz, P. Shafer, E. Arenholz, V. A. Stoica, S. L. Hsu, B. Wang, C. Ophus, J. F. Liu, C. T. Nelson, S. Saremi, B. Prasad, A. B. Mei, D. G. Schlom *et al.*, Observation of room-temperature polar skyrmions, Nature (London) **568**, 368 (2019).

[7] R. Ahluwalia, A. K. Tagantsev, P. Yudin, N. Setter, N. Ng, and D. J. Srolovitz, Influence of flexoelectric coupling on domain patterns in ferroelectrics, Phys. Rev. B **89**, 174105 (2014).

[8] L. Jiang, Y. Zhou, Y. Zhang, Q. Yang, Y. Gu, and L.-Q. Chen, Polarization switching of the incommensurate phases induced by flexoelectric coupling in ferroelectric thin films, Acta Mater. **90**, 344 (2015).

[9] H. Pöttker and E. K. H. Salje, Flexoelectricity, incommensurate phases and the Lifshitz point, J. Phys.: Condens. Matter **28**, 075902 (2016).

[10] T. A. Aslanian and A. P. Levanyuk, Possibility of the incommensurate phase near Alpha-reversible-beta transition point in quartz, Solid State Commun. **31**, 547 (1979).

[11] E. Snoeck, A. Lubk, and C. Magén, *Structural Characterization of Ferroelectric and Multiferroic Nanostructures by Advanced TEM Techniques* (John Wiley & Sons, New York, 2016), Chap. 10, pp. 275–324.

[12] Z. L. Luo, H. Huang, H. Zhou, Z. H. Chen, Y. Yang, L. Wu, C. Zhu, H. Wang, M. Yang, S. Hu, H. Wen, X. Zhang, Z. Zhang, L. Chen, D. D. Fong, and C. Gao, Probing the domain structure of $BiFeO_3$ epitaxial films with three-dimensional reciprocal space mapping, Appl. Phys. Lett. **104**, 182901 (2014).

[13] J. Chrosch and E. K. H. Salje, Temperature dependence of the domain wall width in $LaAlO_3$, J. Appl. Phys. **85**, 722 (1999).

[14] C. Noguera, Polar oxide surfaces, J. Phys.: Condens. Matter **12**, R367 (2000).

[15] J. Goniakowski, F. Finocchi, and C. Noguera, Polarity of oxide surfaces and nanostructures, Rep. Prog. Phys. **71**, 016501 (2008).

[16] B. Houchmandzadeh, J. Lajzerowicz, and E. Salje, Order parameter coupling and chirality of domain-walls, J. Phys.: Condens. Matter **3**, 5163 (1991).

[17] B. Houchmanzadeh, J. Lajzerowicz, and E. Salje, Interfaces and ripple states in ferroelastic crystals—a simple model, Phase Transit. **38**, 77 (1992).

[18] V. K. Lazarov, S. A. Chambers, and M. Gajdardziska-Josifovska, Polar Oxide Interface Stabilization by Formation of Metallic Nanocrystals, Phys. Rev. Lett. **90**, 216108 (2003).

[19] S. Hong, S. M. Nakhmanson, and D. D. Fong, Screening mechanisms at polar oxide heterointerfaces, Rep. Prog. Phys. **79**, 076501 (2016).

[20] D. Di Sante, P. Barone, R. Bertacco, and S. Picozzi, Electric control of the giant Rashba effect in bulk GeTe, Adv. Mater. **25**, 509 (2013).

[21] A. V. Kolobov, D. J. Kim, A. Giussani, P. Fons, J. Tominaga, R. Calarco, and A. Gruverman, Ferroelectric switching in epitaxial GeTe films, APL Mater. **2**, 066101 (2014).

[22] C. Rinaldi, S. Varotto, M. Asa, J. Slawinska, J. Fujii, G. Vinai, S. Cecchi, D. Di Sante, R. Calarco, I. Vobornik, G. Panaccione, S. Picozzi, and R. Bertacco, Ferroelectric control of the spin texture in GeTe, Nano Lett. **18**, 2751 (2018).

[23] J. Krempasky, S. Muff, J. Minar, N. Pilet, M. Fanciulli, A. P. Weber, E. B. Guedes, M. Caputo, E. Mueller, V. V. Volobuev, M. Gmitra, C. A. F. Vaz, V. Scagnoli, G. Springholz, and J. H. Dil, *Operando* Imaging of All-Electric Spin Texture Manipulation in Ferroelectric and Multiferroic Rashba Semiconductors, Phys. Rev. X **8**, 021067 (2018).

[24] R. Wang, J. E. Boschker, E. Bruyer, D. Di Sante, S. Picozzi, K. Perumal, A. Giussani, H. Riechert, and R. Calarco, Toward truly single crystalline GeTe films: The relevance of the substrate surface, J. Phys. Chem. C **118**, 29724 (2014).

[25] B. Croes, F. Cheynis, Y. Zhang, C. Voulot, K. D. Dorkenoo, S. Cherifi-Hertel, C. Mocuta, M. Texier, T. Cornelius, O. Thomas, M.-I. Richard, P. Mueller, S. Curiotto, and F. Leroy, Ferroelectric nanodomains in epitaxial GeTe thin films, Phys. Rev. Materials **5**, 124415 (2021).

[26] C. Mocuta, M.-I. Richard, J. Fouet, S. Stanescu, A. Barbier, C. Guichet, O. Thomas, S. Hustache, A. V. Zozulya, and D. Thiaudiere, Fast pole figure acquisition using area detectors at the DiffAbs beamline—Synchrotron SOLEIL, J. Appl. Cryst. **46**, 1842 (2013).

[27] Y. Liu, Y. Y. Li, S. Rajput, D. Gilks, L. Lari, P. L. Galindo, M. Weinert, V. K. Lazarov, and L. Li, Tuning Dirac states by strain in the topological insulator $Bi_2Se_3$, Nat. Phys. **10**, 294 (2014).

[28] W. X. Tang, K. L. Man, H. C. Huang, C. H. Woo, and M. S. Altman, Growth shapes of Ag crystallites on the Si(111) surface, J. Vac. Sci. Technol. B **20**, 2492 (2002).

[29] D. Kriegner, G. Springholz, C. Richter, N. Filet, E. Mueller, M. Capron, H. Berger, V. Holy, J. H. Dil, and J. Krempasky, Ferroelectric self-poling in GeTe films and crystals, Crystals **9**, 335 (2019).

[30] See Supplemental Material at https://link.aps.org/supplemental/10.1103/PhysRevMaterials.6.064407 for a comparison of GeTe thin film surface morphologies by LEEM and STM.

[31] M. Giesen, Step and island dynamics at solid/vacuum and solid/liquid interfaces, Prog. Surf. Sci. **68**, 1 (2001).

[32] A. S. Frolov, J. Sanchez-Barriga, C. Callaert, J. Hadermann, V. A. Fedorov, D. Y. Usachov, A. N. Chaika, B. C. Walls, K. Zhussupbekov, V. I. Shvets, M. Muntwiler, M. Amati, L.

Gregoratti, A. Y. Varykhalov, O. Rader, and V. L. Yashina, Atomic and electronic structure of a multidomain GeTe crystal, ACS Nano **14**, 16576 (2020).

[33] V. L. Deringer, M. Lumeij, and R. Dronskowski, Ab initio modeling of alpha-GeTe(111) surfaces, J. Phys. Chem. C **116**, 15801 (2012).

[34] E. C. Sowa, M. A. VanHove, and D. L. Adams, The missing-row model for the reconstructed Pt(110)-(1×2) Surface—A LEED intensity analysis showing multilayer distortions, Surf. Sci. **199**, 174 (1988).

[35] I. K. Robinson, Direct Determination of the Au(110) Reconstructed Surface by X-Ray Diffraction, Phys. Rev. Lett. **50**, 1145 (1983).

[36] H. Tanaka, J. Yoshinobu, and M. Kawai, Oxygen-induced reconstruction of the Pd(110) surface—an STM study, Surf. Sci. **327**, L505 (1995).

[37] K. Nakajima, K. Kimura, and M. Mannami, The (111) surface of PbTe observed by high-resolution RES, Nucl. Instrum. Methods Phys. Res. Sect. B **135**, 350 (1998).

[38] F. Finocchi, A. Barbier, J. Jupille, and C. Noguera, Stability of Rocksalt (111) Polar Surfaces: Beyond the Octopole, Phys. Rev. Lett. **92**, 136101 (2004).

[39] C. Franchini, V. Bayer, R. Podloucky, G. Parteder, S. Surney, and F. P. Netzer, Density functional study of the polar MnO(111) surface, Phys. Rev. B **73**, 155402 (2006).

[40] J. V. Lauritsen, S. Porsgaard, M. K. Rasmussen, M. C. R. Jensen, R. Bechstein, K. Meinander, B. S. Clausen, S. Helveg, R. Wahl, G. Kresse, and F. Besenbacher, Stabilization principles for polar surfaces of ZnO, ACS Nano **5**, 5987 (2011).

[41] A. Ohtake, J. Nakamura, T. Komura, T. Hanada, T. Yao, H. Kuramochi, and M. Ozeki, Surface structures of GaAs{111}A, B-(2×2), Phys. Rev. B **64**, 045318 (2001).

[42] D. Wolf, Reconstruction of NaCl Surfaces from a Dipolar Solution to the Madelung Problem, Phys. Rev. Lett. **68**, 3315 (1992).

[43] J. Fuchs, Z. Feit, and H. Preier, Reflection high-energy electron-diffraction intensity oscillations in IV-VI compound semiconductors, Appl. Phys. Lett. **53**, 894 (1988).

[44] H. Wu, J. Si, Y. Yan, Q. Liao, and Y. Lu, Reconstructions and stabilities of PbTe(111) crystal surface from experiments and density-functional theory, Appl. Surf. Sci. **356**, 742 (2015).

[45] K. M. Yu, A. Locatelli, and M. S. Altman, Comparing Fourier optics and contrast transfer function modeling of image formation in low energy electron microscopy, Ultramicroscopy **183**, 109 (2017).

[46] M. V. Molchanov, A. S. Alikhanyan, V. P. Zlomanov, and L. V. Yashina, Mass spectrometric study of vapor composition over germanium telluride, Inorg. Mater. **38**, 559 (2002).

[47] R. F. Brebrick, Partial pressures and high-temperature thermodynamic properties for the germanium-tellurium system, J. Phase Equilib. Diffus. **40**, 291 (2019).